RSC Advances

PAPER

View Article Online
View Journal | View Issue

Cite this: *RSC Adv.*, 2026, **16**, 4667

Fabrication of a Z-scheme 3D/2D $MgIn_2S_4$/BiOBr heterojunction for enhanced photocatalytic removal of ciprofloxacin in water

Tunde Lewis Yusuf, *[ad] Damilola Caleb Akintayo, [a] Peter Osazuwa,[b] Michael Uzu [c] and Foluso Oyedotun Agunbiade *[d]

Engineered Z-scheme semiconductor systems offer promising strategies for the removal of antibiotics from contaminated water. Here, we report the fabrication of a Z-scheme heterojunction by coupling two-dimensional (2D) bismuth oxybromide (BiOBr) nanosheets with three-dimensional (3D) magnesium indium sulfide ($MgIn_2S_4$) nanoflowers to enhance the photocatalytic degradation of ciprofloxacin (CIP) under visible light irradiation. The BiOBr/$MgIn_2S_4$ composite was synthesized through a simple *in situ* hydrothermal method, and comprehensive characterization techniques, including X-ray diffraction (XRD), field-emission scanning electron microscopy (FESEM), and transmission electron microscopy (TEM), confirmed the successful formation of a highly intimate 2D/3D heterojunction. Among the various composites, the BiOBr/30%$MgIn_2S_4$ heterojunction exhibited the highest CIP degradation efficiency, achieving 89.9% within 60 minutes, significantly outperforming the pristine BiOBr (52.6%) and $MgIn_2S_4$ (58.5%) under visible light. This remarkable enhancement in photocatalytic activity is attributed to the synergistic effects of improved visible light absorption and, more critically, efficient charge separation, as evidenced by photoelectrochemical measurements and photoluminescence spectroscopy. X-ray photoelectron spectroscopy (XPS), Mott–Schottky analysis, and radical trapping experiments provided conclusive evidence for a Z-scheme charge transfer mechanism. This mechanism facilitates the spatial separation of charge carriers, where oxidative holes in the valence band of BiOBr are preserved for direct CIP oxidation and hydroxyl radical ($^{\bullet}OH$) generation, while the reductive electrons in the conduction band of $MgIn_2S_4$ drive the generation of superoxide radicals ($O_2^{\bullet-}$). Moreover, the composite demonstrated excellent reusability, maintaining its performance over five consecutive cycles. These findings offer valuable insights into the design and optimization of efficient 2D/3D Z-scheme photocatalysts for advanced environmental remediation applications, particularly in the removal of organic contaminants from water.

Received 15th October 2025
Accepted 27th December 2025

DOI: 10.1039/d5ra07896b

rsc.li/rsc-advances

1 Introduction

The persistent contamination of global water resources by pharmaceutical pollutants represents a critical environmental challenge of the 21st century.[1–3] Among these contaminants, antibiotics pose a particular threat due to their biological activity, persistence, and role in promoting antimicrobial resistance.[4] Ciprofloxacin (CIP), a second-generation fluoroquinolone antibiotic,[5] is among the most frequently detected antibiotics in water systems due to its broad-spectrum efficacy and high consumption.[6] Its stable molecular structure, characterized by a piperazinyl ring and a quinolone moiety, makes it recalcitrant to natural degradation and conventional treatment methods like adsorption, coagulation, and biological processes.[7] These methods often transfer the pollutant to another phase (such as sludge) rather than mineralizing it, creating a secondary waste problem.[8] Consequently, there is an urgent and critical need to develop advanced, efficient, and sustainable technologies for the complete removal of CIP and other antibiotic residues from water.

Heterogeneous photocatalysis has emerged as a promising advanced oxidation process (AOPs) for antibiotic degradation, utilizing solar energy to generate reactive oxygen species that can mineralize organic pollutants.[9] Typically, AOPs are based on the *in situ* generation of reactive oxygen species (ROS), such as holes (h^+), hydroxyl radicals ($^{\bullet}OH$), and superoxide anions ($O_2^{\bullet-}$), which can non-selectively oxidize and mineralize

[a]*Department of Chemistry, Faculty of Natural and Agricultural Sciences, University of Pretoria, Private Bag X20, Hatfield, Pretoria 0028, South Africa. E-mail: yusuf.tl@up.ac.za*

[b]*Laboratory of Molecular Science and Engineering and the Laboratory of Natural Materials Technology, Faculty of Science and Engineering, Åbo Akademi University, Finland*

[c]*Department of Chemistry and Biochemistry, University of Delaware, USA*

[d]*Department of Chemistry, Faculty of Physical and Earth Sciences, University of Lagos, Akoka-Yaba, Lagos, Nigeria. E-mail: fagunbiade@unilag.edu.ng*

complex organic pollutants into harmless end products like CO_2 and H_2O.[10] However, the efficiency of this process is fundamentally affected by three key factors: rapid recombination of photogenerated charge carriers, limited visible-light absorption, and insufficient redox potential in single-component photocatalysts.[11] While various strategies have been developed to overcome these issues, the construction of heterojunction photocatalysts with aligned band structure has demonstrated its effectiveness in enhancing charge separation through interfacial engineering.[12–14] Traditionally, a type-II heterojunction is formed, where the band edges are staggered. This allows photogenerated electrons to migrate to the semiconductor with the conduction band (CB) that is more positive, while holes transfer to the semiconductor with the valence band (VB) that is more negative. While this spatial separation reduces recombination, the electrons and holes accumulate on less negative CB and less positive VB, respectively, significantly weakening their redox abilities.[15,16] This trade-off between charge separation and redox power is a fundamental drawback of the type-II mechanism for degrading highly stable pollutants like CIP, which require strong oxidative potential. Therefore, using the type-II band alignment, a Z-scheme heterojunction simultaneously achieves superior spatial charge separation and maintains the strongest possible redox potentials, making it ideal for photocatalytic reactions such as pollutant degradation.[17,18]

Moreover, the selection of appropriate semiconductors is important for constructing an efficient Z-scheme system. BiOBr, a two-dimensional (2D) p-type semiconductor, has attracted considerable attention due to its unique layered structure, chemical stability, and appropriate valence band position with strong oxidative capability.[19] However, its wide band gap restricts visible light absorption.[20] On the other hand, $MgIn_2S_4$ is a three-dimensional (3D) n-type semiconductor, which is visible-light-driven with a narrower band gap and excellent chemical stability. Its more negative conduction band position is suitable for reduction reactions.[21,22] Individually, both materials suffer from rapid charge recombination. However, their complementary band structures and opposite semiconductor types (p–n) make them ideal candidates for forming a heterojunction. Furthermore, 2D nanomaterials offer exceptional advantages, including abundant active sites, high surface-to-volume ratios, and short charge migration paths.[23] Their structure facilitates strong interfacial contact with other components and provides enhanced accessibility to reaction sites.[24] Conversely, 3D hierarchical structures provide robust frameworks with improved light harvesting through multiple scattering effects, enhanced mass transfer capabilities, and better structural stability.[25] Therefore, the construction of a 2D/3D interface between BiOBr nanosheets and $MgIn_2S_4$ microspheres offers a large contact area, facilitating efficient interfacial charge transfer and providing abundant surface-active sites.

Heterojunctions such as CdS/BiOBr,[26] BiOBr/Bi_2O_2S,[27] SnO_2/BiOBr,[28] $MgIn_2S_4$/CdS,[29] g-C_3N_4/$MgIn_2S_4$,[22] BN/$Zn_3In_2S_6$,[30] $W_{18}O_{49}$/Bi_4NbO_8Cl,[31] and so on, have been constructed for the treatment of organic pollutants in water. Herein, we proposed a rational design and synthesis of a 2D/3D BiOBr/$MgIn_2S_4$ Z-scheme heterojunction photocatalyst for the enhanced degradation of Ciprofloxacin. We systematically investigate the synthesis, optical properties, morphology, and photocatalytic performance of the BiOBr/$MgIn_2S_4$ composite. Through a combination of spectroscopic techniques and radical trapping experiments, we provide evidence for the Z-scheme charge transfer mechanism. This study not only presents an efficient photocatalyst for mitigating antibiotic pollution but also offers insights into the electronic principles governing charge dynamics in advanced heterojunction systems, paving the way for the rational development of advanced photocatalysts.

2 Experimental section

2.1 Materials used

Bismuth nitrate pentahydrate ($Bi(NO_3)_3$ $6H_2O$), sodium hydroxide (NaOH), L-cysteine, magnesium nitrate hexahydrate ($Mg(NO_3)_2$ $6H_2O$), deionized water, indium chloride ($InCl_3$), ethanol, potassium hexacyanoferrate (II) ($K_4Fe(CN)_6$), polyvinylidene fluoride (PVDF), ethylenediaminetetraacetic acid disodium salt (Na_2EDTA), silver nitrate ($AgNO_3$), p-Acrylamide(AA), isopropanol (IPA), Ciprofloxacin (CIP), potassium chromate ($K_2Cr_2O_7$), potassium hexacyanoferrate (III) ($K_3Fe(CN)_6$), and N-methyl-2-pyrrolidone (NMP) were used for this study and purchased from Sigma-Aldrich (South Africa).

2.2 Synthesis of bismuth oxybromide (BiOBr)

The BiOBr nanosheets were prepared *via* a hydrothermal approach using the synthesis approach described by Lixin *et al.*[32] In this process, $Bi(NO_3)_3$. $5H_2O$ (0.002 mol) and potassium bromide (0.0021 mol) were dissolved in 50 mL of deionised H_2O and sonicated for 30 min. The resulting solution was subjected to hydrothermal treatment for 24 h at 180 °C. After cooling, the synthesised product was washed repeatedly with deionised H_2O and ethanol before drying for 8 h.

2.3 Synthesis of magnesium indium sulfide ($MgIn_2S_4$)

A mixture containing 0.2 mmol of magnesium nitrite hexahydrate ($Mg(NO)_2 \cdot 6H_2O$), indium(III) chloride 0.4 mmol, L-cysteine (0.9 mmol) was prepared in a beaker. The solution was stirred for one hour before transferring to a Teflon-lined autoclave. The autoclave was then placed in a furnace and heated for 24 h at 180 °C. After the reaction, the resulting solid was separated *via* centrifugation and thoroughly washed three times with both deionized water and ethanol. Finally, the product was dried for eight hours at 70 °C to obtain pure $MgIn_2S_4$.[33]

2.4 Synthesis of BiOBr/$MgIn_2S_4$

The hydrothermal *in situ* method was employed to synthesize the heterojunction. Different mole ratios (10%, 20%, 30%, and 50%) of the as-synthesized $MgIn_2S_4$ were weighed and dispersed into four separate beakers, each containing 20 mL of deionized water. The mixtures were sonicated for 1 hour to ensure

uniform dispersion. Subsequently, BiOBr was synthesized in each beaker following the procedure described in Section 2.2.

2.5 Characterisation and instruments

The detailed procedures of the instruments used for characterisation are listed in the SI section.

2.6 Photocatalytic degradation experiments

Photocatalytic degradation tests were conducted using a 100 W Xenon solar lamp as the light source, placed at a fixed distance of 10 cm from the solution. In a typical procedure, 40 mg of the synthesized catalyst was added to 50 mL of an aqueous ciprofloxacin (CIP) solution (10 mg L^{-1}, pH 7). This suspension was first stirred in the dark for 20 minutes to allow the system to reach adsorption–desorption equilibrium. Upon turning the lamp on, 3 mL aliquots were withdrawn at scheduled time intervals. The solid catalyst was subsequently separated from these samples by centrifugation (7000 rpm, 10 min), and the supernatant was examined. The residual ciprofloxacin (CIP) concentration was quantified using a UV-Vis spectrophotometer at 278 nm to evaluate photocatalytic efficiency at 10-minute intervals. To assess the reusability and stability of the catalyst, successive photocatalytic degradation cycles were performed under identical conditions. After each cycle, the catalyst was recovered by centrifugation, washed thoroughly with deionized water and ethanol to remove any adsorbed intermediates, dried at 60 °C overnight, and reused in the subsequent run. The degradation efficiency was monitored over five consecutive cycles.

The degradation efficiency was calculated using eqn 1

$$\%\ \text{Degradation efficiency} = \left(1 - \frac{C_t}{C_0}\right) \times 100 \quad (1)$$

2.7 Radical trapping experiment

The major reactive species participating in the oxidation mechanism were investigated through radical trapping experiments. Specific scavengers (2 mM each) were introduced to selectively inhibit different active intermediates: isopropanol (IPA) for hydroxyl radicals ($^{\bullet}OH$), Acrylamides (AA) for superoxide radicals ($O_2^{\bullet -}$), and sodium EDTA for photogenerated holes (h^+), these controlled trapping experiments helped elucidate the predominant pathways involved in the photocatalytic degradation process.

3 Results and discussion

3.1 Structural and morphological studies

The structural properties and crystalline phases of the synthesised materials were confirmed using the XRD analysis. As displayed in Fig. 1a, the diffraction peaks of $MgIn_2S_4$ at peak positions: 14.07°, 23.23°, 27.42°, 28.88°, 33.18°, 43.57°, 47.79°, 56.09°, 59.43° & 66.72° correspond to the *hkl* (111), (220), (311), (222), (400), (333), (440), (533), (444), & (731) planes, respectively, confirming the cubic phase of $MgIn_2S_4$ (JCPDS No. 04-007-9835). The synthesised BiOBr shows characteristics peaks at 10.76°, 21.79°, 25.05°, 31.59°, 32.10°, 40.43°, 44.62°, 46.12°, 50.60°, 53.27°, 56.11°, 57.06°, 70.96°, & 76.58° which are well indexed to the *hkl* planes (001), (002), (101), (102), (110), (103), (004), (103), (200), (104), (211), (114), (212), (006) & (310) of the tetragonal phase BiOBr (JCPDS No. 00-009-0393). The spectra show minimal peak broadening, thus indicating good crystallinity. In the BiOBr/$MgIn_2S_4$ composite, the XRD diffraction pattern showed the combination of peaks from both BiOBr and $MgIn_2S_4$ without additional phase, confirming the successful synthesis of a heterojunction rather than a new compound. However, a minor 2θ shift (>0.5°) was observed in the (111) and (222) planes of $MgIn_2S_4$ in BiOBr/$MgIn_2S_4$, which can be attributed to interfacial strain[34], because of the synthesis method.

In addition, the crystallite sizes of the photocatalysts were determined using the Scherrer equation (eqn (2))[35] and the data extracted from the XRD analysis (Table S1)

$$D = \frac{K\lambda}{\beta \cos \theta} \quad (2)$$

where λ = X-ray wavelength (usually 0.1540 nm for Cu-Kα radiation), $K = 0.9$ for materials (a factor), θ = Peak diffraction angle (in radians), D = Crystallite size and β = Full width at half maximum (FWHM, in radians). The calculated average crystallite sizes for BiOBr, $MgIn_2S_4$, and BiOBr/$MgIn_2S_4$ composite were 322.67 nm, 93.63 nm & 287.74 nm, respectively. Materials with smaller crystallites offer high surface area and more active sites but experience increased recombination due to short diffusion length, while larger crystallite enhances crystallinity and charge transport but tend to reduce surface reactivity.[36] Therefore, the BiOBr/$MgIn_2S_4$ composite with reduced crystallite size from 322.67 nm in $MgIn_2S_4$, combines the surface activity of BiOBr and the charge mobility of $MgIn_2S_4$ to form a heterojunction with improved charge separation and enhanced photocatalytic activity.

The surface morphology of the photocatalysts was examined using FESEM. As displayed in Fig. 1b, the BiOBr micrograph shows a hierarchical morphology of nanosheets assembled into a flower-like microstructure. These nanosheets are loosely stacked and layered, which favours surface redox reaction.[22] On the other hand, the $MgIn_2S_4$ micrograph (Fig. 1c) displays a well-defined three-dimensional (3D) microsphere that is made up of interconnected nanoflakes. This morphology offers rough surface texture and high porosity, which are beneficial for visible light harvesting and easy charge transport.[25] In the BiOBr/$MgIn_2S_4$ composite (Fig. 1d), a mixed morphology is observed where the BiOBr nanosheets are uniformly anchored onto the surface of the $MgIn_2S_4$ nanoflakes, resulting in a well-integrated 2D/3D heterostructure with strong interfacial interaction, improved light harvesting, and effective charge mobility, which affects the overall degradation efficiency.

Furthermore, the TEM micrographs of BiOBr (Fig. 1e) also reveal the nanosheet-like structure in a loosely and layered arrangement, while the $MgIn_2S_4$ micrograph (Fig. 1f) reveals a dense spherical structure composed of interconnected flakes. Similarly, the TEM image of BiOBr/$MgIn_2S_4$ shown in Fig. 1g

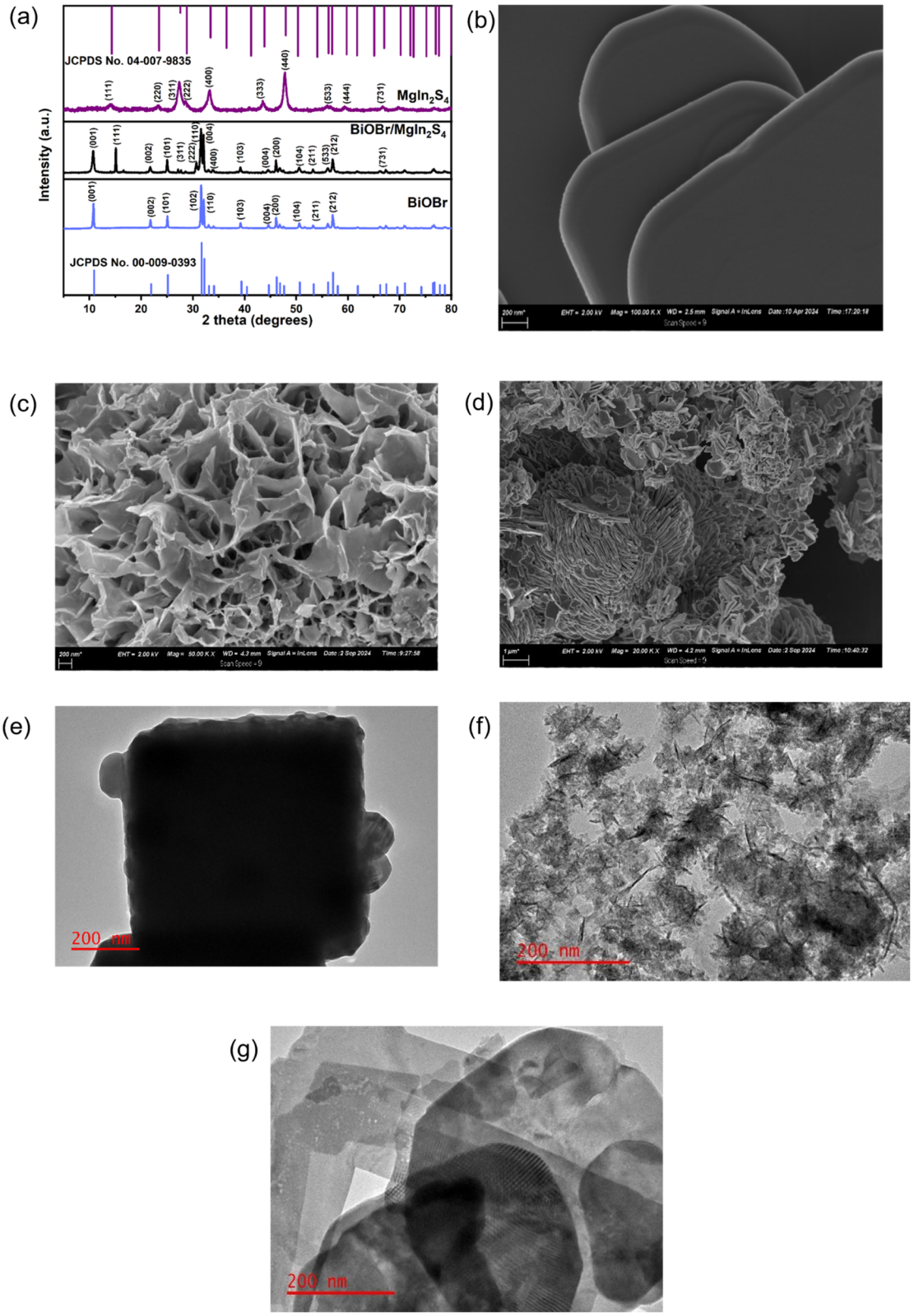

Fig. 1 (a) XRD diffraction pattern of BiOBr, $MgIn_2S_4$ & $BiOBr/MgIn_2S_4$. FESEM micrograph of (b) BiOBr, (c) $MgIn_2S_4$, (d) $BiOBr/MgIn_2S_4$. TEM micrograph of (e) BiOBr, (f) $MgIn_2S_4$ (g) $BiOBr/30\%MgIn_2S_4$.

confirms the interfacial interaction between BiOBr and $MgIn_2S_4$, with some areas showing lattice fringes, thus confirming the crystallinity of the material.[37]

3.2 Elemental composition

The chemical states and surface composition of the as-synthesized BiOBr, $MgIn_2S_4$ & BiOBr/$MgIn_2S_4$ were investigated using XPS measurement. The survey scan (Fig. S1) confirms the presence of bismuth, oxygen, bromine, and magnesium, indium, and sulphur in BiOBr, $MgIn_2S_4$, and BiOBr/$MgIn_2S_4$. Furthermore, the spectra of Bi 4f, Mg 1s, O 1s, Br 3d, In 3d, & S 2p were further investigated to verify the oxidation states and investigate any binding energy shifts associated with interfacial electronic interactions. The Bi 4f spectra (Fig. 2a) show two peaks of Bi $4f_{7/2}$ & Bi $4f_{5/2}$ at binding energies of 159.2 eV & 164.6 eV for BiOBr, which shifted to 159.5 eV & 164.9 eV for BiOBr/$MgIn_2S_4$. Also, the O 1s spectra (Fig. 2b) show two peaks at 530.2 eV & 531.6 eV for BiOBr, which correspond to the lattice oxygen (Metal–Oxygen bond) and are shifted to 530.3 eV & 531.9 eV in BiOBr/$MgIn_2S_4$. Furthermore, the Br 3d spectra (Fig. 2c) show a peak at a binding energy of 68.4 eV in BiOBr and 68.8 eV in BiOBr/$MgIn_2S_4$. On the other hand, the Mg 1s spectra (Fig. 2d) show a peak at a binding energy of 1303.6 eV for $MgIn_2S_4$ and 1302.7 eV for BiOBr/$MgIn_2S_4$. The In 3d spectra (Fig. 2e) show two peaks that correspond to In 3d5/2 and 3d3/2 at binding energies of 444.4 eV & 452.0 eV for $MgIn_2S_4$ and 442.7 eV & 452.9 eV for BiOBr/$MgIn_2S_4$, respectively. Finally, the S 2p spectra (Fig. 2f) show two peaks, which are attributed to S 2p3/2 & 2p1/2 at binding energies of 161.1 eV & 164.2 eV for $MgIn_2S_4$, and 159.5 eV and 164.7 eV for BiOBr/$MgIn_2S_4$, respectively.

In summary, upon the formation of BiOBr/$MgIn_2S_4$ heterojunction, the core level positions of all elements undergo positive and negative shifts relative to the pristine semiconductors. As clearly illustrated in Table 1, the Bi 4f, O 1s & Br 3d shift to a higher binding energy from BiOBr to BiOBr/$MgIn_2S_4$. Likewise, the Mg 1s, In 3d & S 2p shift to lower binding energy from $MgIn_2S_4$ to BiOBr/$MgIn_2S_4$, although with minor deviation in the In $3d_{3/2}$ and S $2p_{1/2}$ orbitals that undergo a shift to higher binding energy. Therefore, this shift suggests that electrons were transferred from BiOBr to $MgIn_2S_4$ upon heterojunction formation. This implies that there is a reduction in electron density around the elements of BiOBr, leading to electron accumulation on the surface of $MgIn_2S_4$. The slight positive shifts observed for In $3d_{3/2}$ and S $2p_{1/2}$ could be attributed to partial surface oxidation of sulphur or indium due to interaction with oxygen.[38]

In all, the XPS results demonstrate that strong electronic interaction occurs at the interface of BiOBr/$MgIn_2S_4$, establishing the formation of an internal electric field and favourable band alignment for effective charge separation.

3.3 Photoelectrochemical properties and optical studies

The Nyquist plots (Fig. 3a), with the equivalent circuit model (Fig. S2), revealed a decrease in charge transfer resistance (R_{ct}) value of BiOBr/$MgIn_2S_4$ (71 Ω) relative to the pristine BiOBr (155 Ω) and $MgIn_2S_4$ (210 Ω). In EIS measurements, the semicircle radius in the high frequency region relates to the R_{ct} at the semiconductor–electrolyte interface.[39] The smaller R_{ct} value observed for BiOBr/$MgIn_2S_4$ indicates that there is more efficient interfacial charge separation and faster electron transfer kinetics. It can be attributed to the strong contact between BiOBr and $MgIn_2S_4$ in the heterojunction formation, thereby leading to suppression of charge recombination of photogenerated carriers.

The transient photocurrent response provided complementary evidence. As shown in Fig. 3b, the BiOBr/30% $MgIn_2S_4$ exhibits photocurrent density of 0.057 mA cm^{-2}, which is the highest, when compared with 0.033 mA cm^{-2}, 0.029 mA cm^{-2}, 0.01 mA cm^{-2}, 0.036 mA cm^{-2}, 0.048 mA cm^{-2} of BiOBr, $MgIn_2S_4$, BiOBr/10% $MgIn_2S_4$, BiOBr/20% $MgIn_2S_4$ & BiOBr/50% $MgIn_2S_4$, respectively. The enhanced photocurrent response of BiOBr/30% $MgIn_2S_4$ can be attributed to the heterostructure formation using the optimal ratio of BiOBr to $MgIn_2S_4$, which promotes efficient charge transfer of photogenerated electrons and holes to the suitable reaction sites while maintaining strong redox potentials. In addition, the stability of the photocurrent over repeated on/off light cycles confirms the photostability of the photocatalyst.

Moreover, the UV-Vis DRS spectra of BiOBr, $MgIn_2S_4$, and different mole ratios of BiOBr/$MgIn_2S_4$ heterojunction are illustrated in Fig. 3c. BiOBr possesses an absorption edge in the ultraviolet region at a wavelength of 471 nm, with limited absorption in the visible region. In contrast, $MgIn_2S_4$ shows strong and broad absorption in the visible light region at a wavelength of 677 nm. Upon the formation of a heterojunction, an increasing ratio of $MgIn_2S_4$ in the composite leads to enhanced visible light absorption. Hence, BiOBr/10% $MgIn_2S_4$, BiOBr/20% $MgIn_2S_4$, and BiOBr/50% $MgIn_2S_4$ exhibit absorption wavelengths of approximately 518 nm, 551 nm, and 659 nm, respectively, while BiOBr/30% $MgIn_2S_4$ possesses an absorption wavelength of 610 nm. Therefore, the broader absorption range is expected to promote higher photogenerated charge carrier density under visible light, leading to enhanced photocatalytic performance.[40]

Furthermore, the photoluminescence spectra (PL) were measured to gain insights into the charge carrier recombination mechanism of the photocatalysts. In general, a strong PL emission corresponds to a fast recombination rate of photogenerated electrons and holes, whereas a weaker PL intensity indicates more efficient charge separation and transfer.[41] As shown in Fig. 3d, pristine BiOBr and $MgIn_2S_4$ exhibited strong PL signals, suggesting fast recombination of charge carriers and limited photocatalytic efficiency. In contrast, the BiOBr/30% $MgIn_2S_4$ heterojunction displayed significantly reduced PL intensity compared with the individual photocatalyst, highlighting its enhanced ability to suppress charge recombination. This observation is consistent with the photocatalytic degradation results and kinetic studies, confirming that the enhanced activity of the heterostructures arises from the efficient charge separation and transfer at the BiOBr/30% $MgIn_2S_4$ interface.

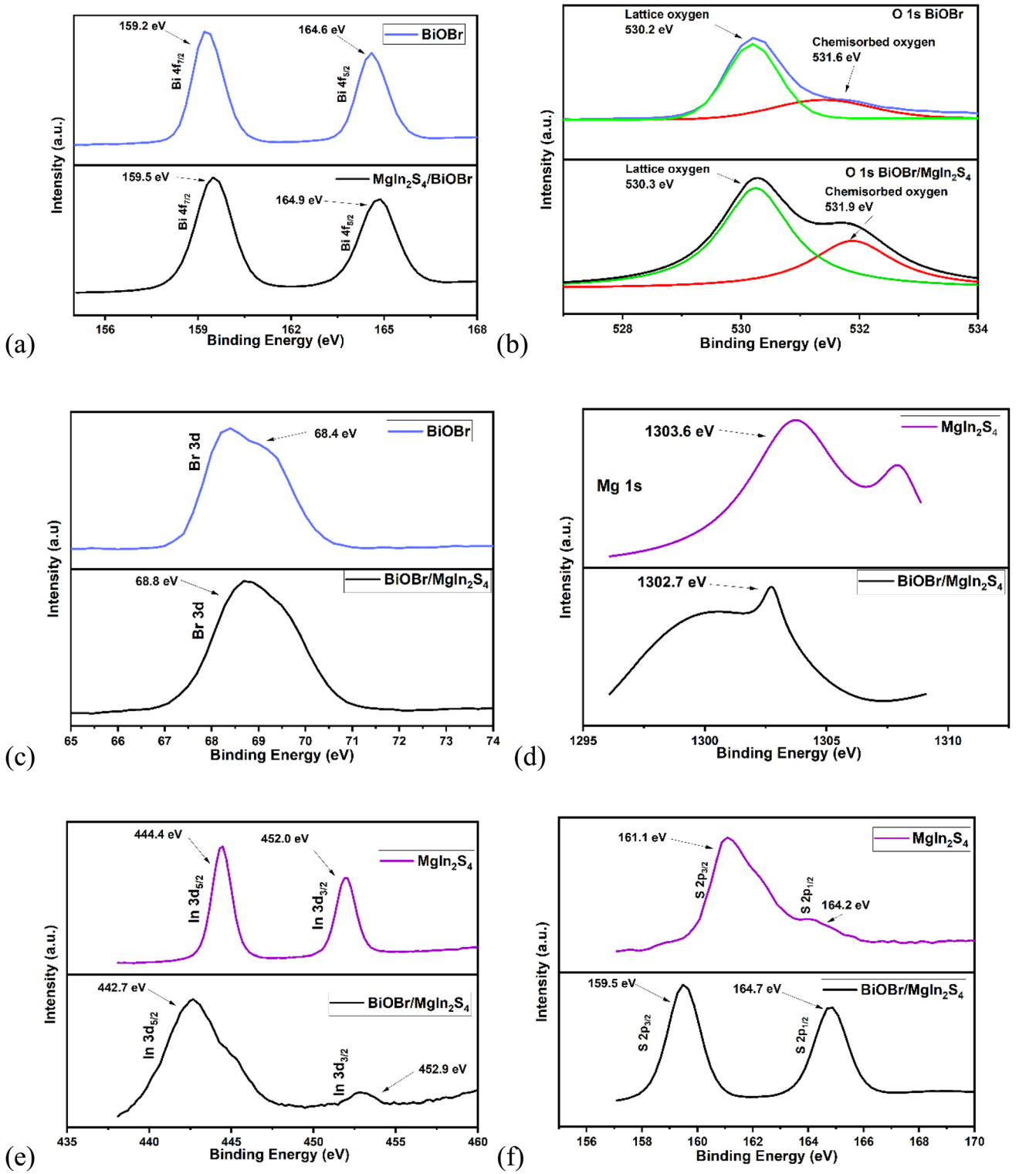

Fig. 2 XPS spectra of (a) Bi 4f, (b) O 1s, (c) Br 3d of BiOBr & BiOBr/$MgIn_2S_4$, (d) Mg 1s, (e) In 3d (f) S 2p of $MgIn_2S_4$ & BiOBr/30%$MgIn_2S_4$.

3.4 Calculation of band energies

The band gap energies of BiOBr and $MgIn_2S_4$ were estimated from the Tauc plots. As shown in Fig. 4a, the extrapolated value for BiOBr is 2.59 eV, while $MgIn_2S_4$ possesses a narrower band gap of 1.78 eV, which is consistent with its strong visible light absorption. The conduction (E_{CB}) and valence band (E_{VB}) energies were calculated using the extrapolated band gap (E_g) values in eqn (4) and (5).

$$E_{CB} = X - E_C - 0.5E_g \quad (3)$$

Table 1 Binding energies of orbitals of BiOBr, $MgIn_2S_4$, and BiOBr/$MgIn_2S_4$

	Binding energy (eV)		
Orbitals	BiOBr	BiOBr/$MgIn_2S_4$	$MgIn_2S_4$
Bi $4f_{7/2}$	159.2	159.5	—
Bi $4f_{5/2}$	164.6	164.9	—
O 1s (M–O)	530.2	530.3	—
O 1s (–OH)	531.6	531.9	—
Br 3d	68.4	68.8	—
Mg 1s	—	1302.7	1303.6
In $3d_{5/2}$	—	442.7	444.4
In $3d_{3/2}$	—	452.9	452.0
S $2p_{3/2}$	—	159.5	161.1
S $2p_{1/2}$	—	164.7	164.2

X is the Mulliken electronegativity, which was calculated to be 6.17 (ref. 42) and 4.68 for BiOBr and $MgIn_2S_4$, respectively. And, E_C is the energy of free electrons on the hydrogen scale, usually 4.5 eV.

Therefore, the E_{CB} & E_{VB} are +0.38 eV & +2.97 eV for BiOBr and −0.71 eV & +1.14 eV for $MgIn_2S_4$, respectively.

Additionally, from the Mott–Schottky analysis, the semiconductor type and flat-band energy (E_{fb} *vs.* Ag/AgCl) were determined. The negative slope observed for BiOBr (Fig. 4b) confirms that it is a p-type semiconductor with E_{fb} value of +0.038 V, while the positive slope observed for $MgIn_2S_4$ (Fig. 4c) confirms that it is an n-type semiconductor with E_{fb} value of −0.97 V. Eqn (3) was used to convert the E_{fb} value to the normal hydrogen electrode standard. Therefore, the E_{fb} (Vs NHE) for BiOBr and $MgIn_2S_4$ are 0.23 eV and −0.78 eV.

$$E_{(NHE)} = E_{(Ag/AgCl)} + 0.194 \quad (4)$$

However, it is assumed that the E_{CB} is more negative E_{fb} with 0.1–0.2 for an n-type semiconductor, while for a p-type semiconductor, the E_{CB} is more positive than the E_{fb}.[43]

Using eqn (4) and (5), taking $\Delta E = 0.1$, the E_{CB} of BiOBr and $MgIn_2S_4$ are +0.33 eV and − 0.88 eV, respectively, which are remarkably close to the calculated values. Therefore, the VB of BiOBr and $MgIn_2S_4$ are 2.92 eV and 0.9 eV, respectively (Fig. 4d).

$$E_{VB} = E_{CB} + E_g \quad (5)$$

$$E_{CB} = E_{fb} - \Delta E \text{ for n-type} \quad (6)$$

$$E_{CB} = E_{fb} + \Delta E \text{ for p-type} \quad (7)$$

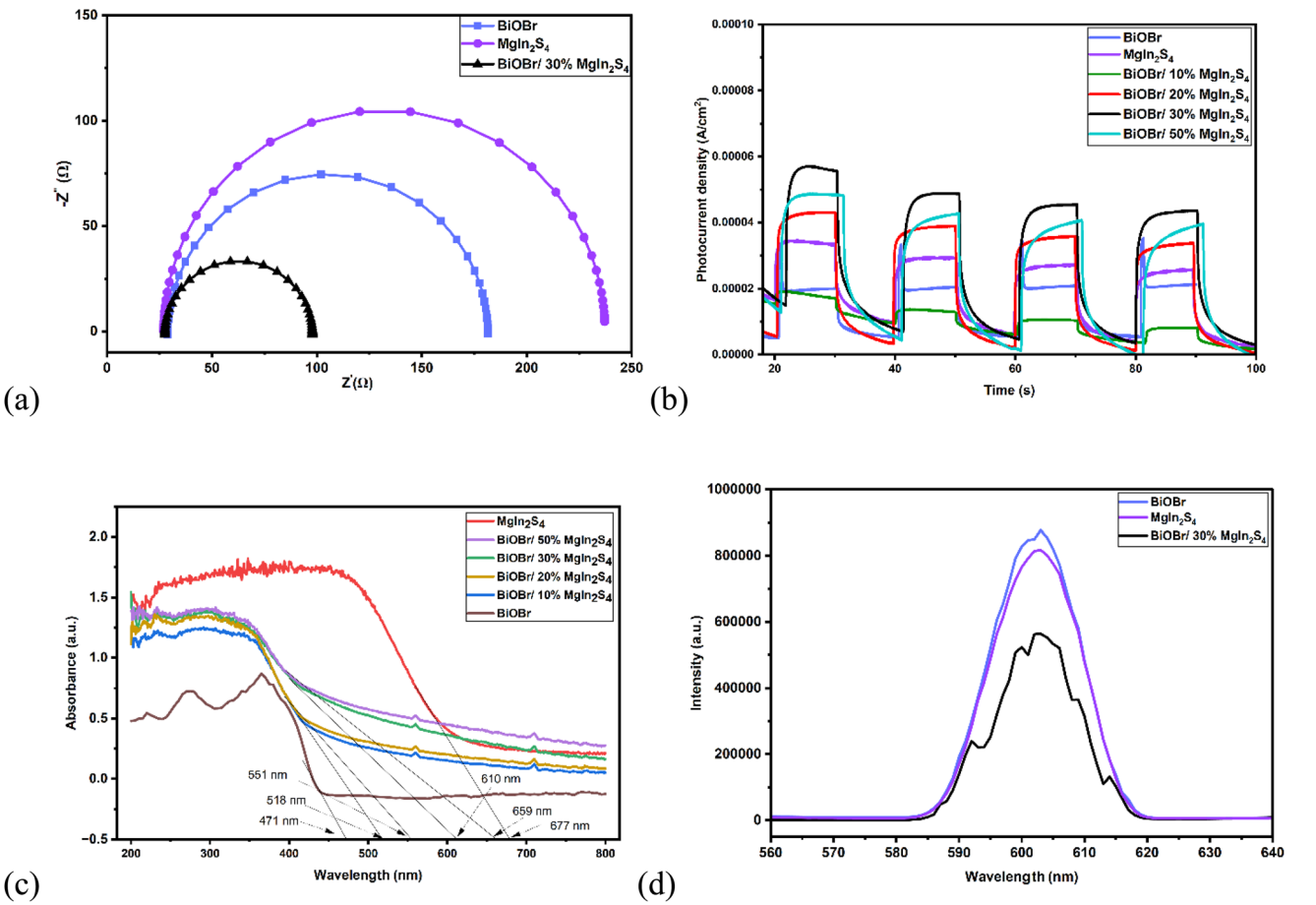

Fig. 3 (a) Nyquist plot of BiOBr, $MgIn_2S_4$ and BiOBr/30% $MgIn_2S_4$ (b) photocurrent response (c)UV-Vis DRS spectra of BiOBr, $MgIn_2S_4$, BiOBr/10% $MgIn_2S_4$, BiOBr/20% $MgIn_2S_4$, BiOBr/30% $MgIn_2S_4$, and BiOBr/50% $MgIn_2S_4$ (d) photoluminescence spectra of BiOBr, $MgIn_2S_4$ and BiOBr/30% $MgIn_2S_4$.

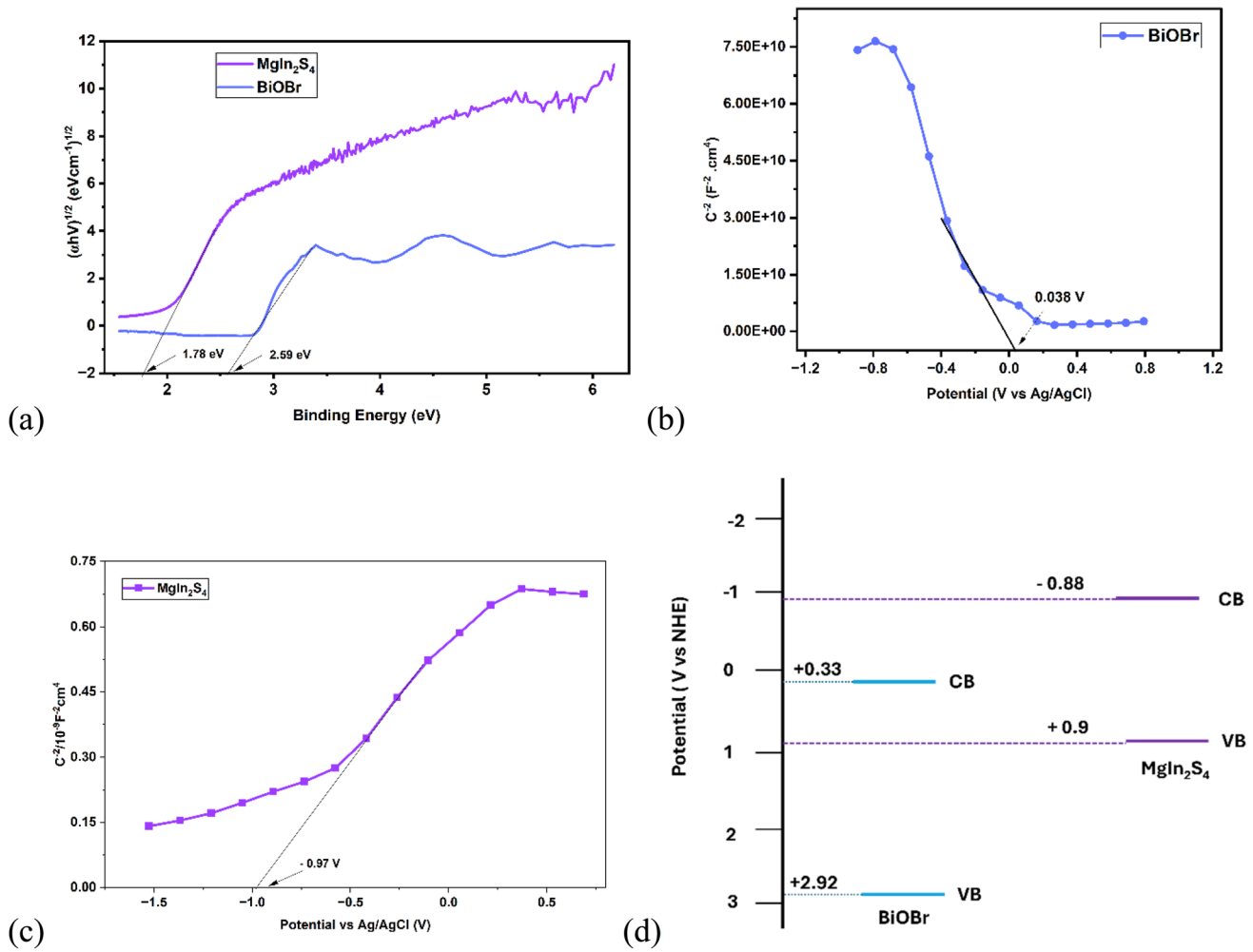

Fig. 4 (a) Tauc plot of BiOBr and $MgIn_2S_4$. Mott Schottky plot (b) BiOBr (c) $MgIn_2S_4$ (d) illustration of band positions of BiOBr and $MgIn_2S_4$.

3.5 Photodegradation, kinetic, reusability, mineralisation studies

The degradation efficiency of the BiOBr/$MgIn_2S_4$ heterojunction was investigated using 10 mg L^{-1} ciprofloxacin (CIP) under visible light irradiation. Prior to illumination, the adsorption equilibrium was evaluated by maintaining the photocatalyst in the pollutant suspension in the dark for 20 min. As shown in Fig. 5a, the adsorption contribution was approximately 10%, 16%, 27%, 27%, 32%, and 27% for BiOBr, $MgIn_2S_4$, BiOBr/10% $MgIn_2S_4$, BiOBr/20% $MgIn_2S_4$, BiOBr/30% $MgIn_2S_4$, & BiOBr/50% $MgIn_2S_4$, respectively. These results indicate that the incorporation of BiOBr into $MgIn_2S_4$ slightly enhances the adsorption capacity, which is likely due to the improved surface affinity and increased surface area of the composites compared with the pristine materials. And the degradation efficiency, when only light was used, was calculated to be 2%.

Upon visible-light irradiation for 60 min, the photocatalytic degradation efficiencies of BiOBr, $MgIn_2S_4$, BiOBr/10% $MgIn_2S_4$, BiOBr/20% $MgIn_2S_4$, BiOBr/30% $MgIn_2S_4$, and BiOBr/50% $MgIn_2S_4$ were calculated to be 52.6%, 58.5%, 80.3%, 84.4%, 89.9%, & 77.6%, respectively. The composite photocatalysts exhibited higher activity than the pristine materials, confirming the synergistic effect of the BiOBr/$MgIn_2S_4$ heterojunction. Notably, the BiOBr/30% $MgIn_2S_4$ heterostructure displayed the highest degradation efficiency, suggesting that an optimal loading of $MgIn_2S_4$ facilitates efficient interfacial charge separation and transfer. However, excessive loading (50%) led to a reduction in performance, which could be attributed to the surface coverage of active sites. These findings demonstrate that band gap tuning of the BiOBr/30% $MgIn_2S_4$ heterojunction composition significantly enhances photocatalytic performance.

To further evaluate the photocatalytic performance, the degradation kinetics of the photocatalyst over the degradation of CIP were analysed using the pseudo-first-order kinetics (eqn (8))

$$\ln\frac{C_t}{C_0} = -kt \quad (8)$$

where k = reaction rate, C_0 and C_t = initial and final concentration of CIP, and t = time of degradation.

As shown in Fig. 5b, the BiOBr/30% $MgIn_2S_4$ exhibited the fastest rate of reaction with the k value 0.031 min^{-1} as compared to BiOBr (0.010 min^{-1}), $MgIn_2S_4$ (0.011 min^{-1}), BiOBr/10% $MgIn_2S_4$ (0.020 min^{-1}), BiOBr/20% $MgIn_2S_4$

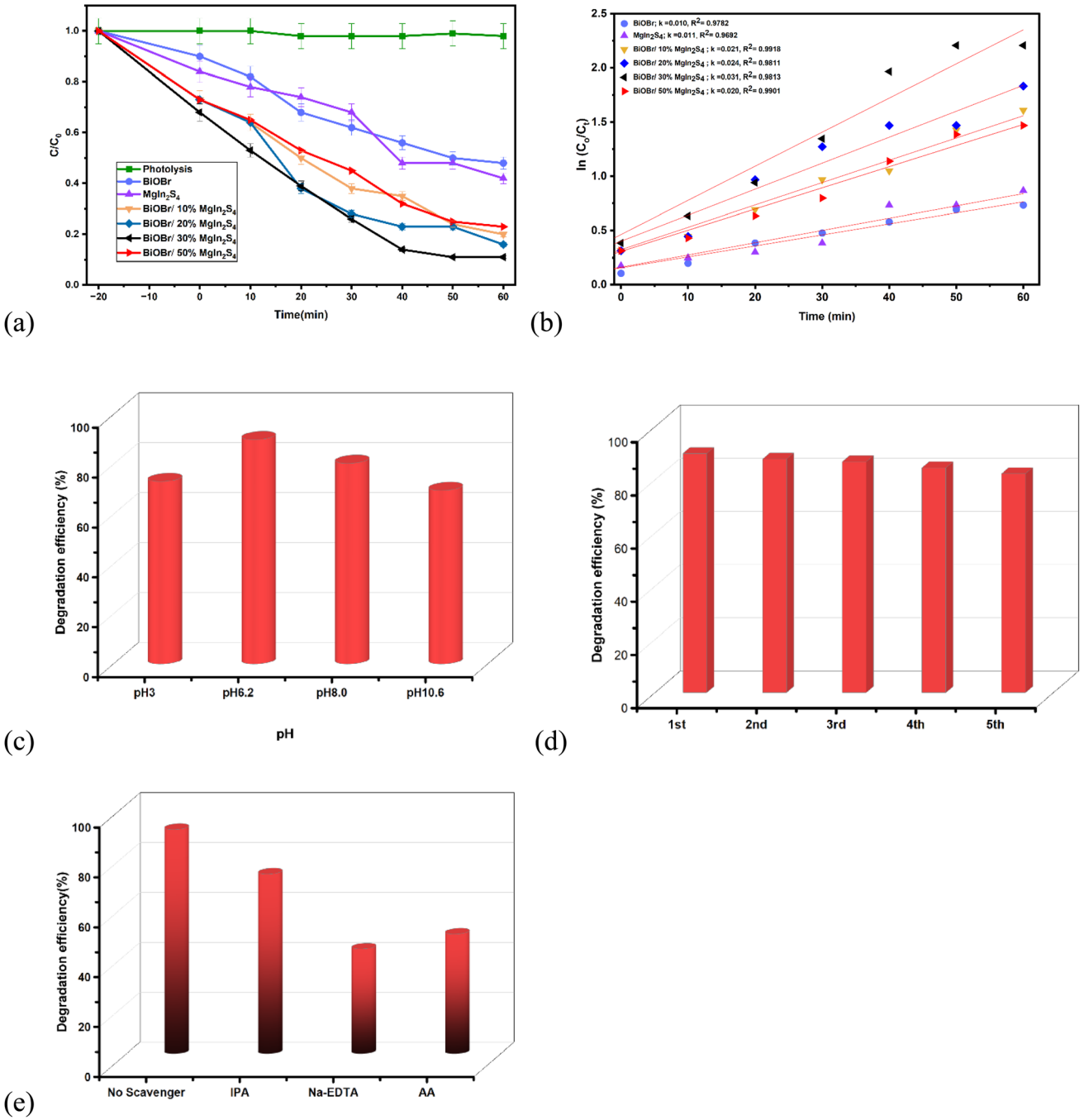

Fig. 5 Degradation plot showing (a) effect of photocatalyst heterojunction, (b) Kinetic studies, (c) effect of pH, (d) stability studies, (e) radical testing (tetracycline 10 mg L^{-1}, 60 min).

(0.019 min^{-1}), & BiOBr/50% $MgIn_2S_4$ (0.019 min^{-1}). The enhanced rate constant reflects the accelerated charge separation and transfer dynamics within the heterojunction, which effectively suppresses electron–hole recombination and promotes the generation of reactive species.

The effect of pH on the photocatalytic degradation of ciprofloxacin was evaluated. As shown in Fig. 5c the maximum efficiency of 89.9% was observed at pH 6.2. Degradation decreased at both acidic (73.1% at pH 3) and alkaline conditions (80.4% at pH 8.0 and 69.5% at pH 10.6), indicating that the photocatalyst exhibits optimal activity under near-neutral conditions. This behaviour is due to the influence of pH on the surface charge of the photocatalyst and the ionization state of the pollutant, affecting adsorption and subsequent degradation.

Moreover, the reusability of the photocatalyst was evaluated over five consecutive cycles of ciprofloxacin degradation (Fig. 5d). The initial cycle exhibited a degradation efficiency of 89.9%, which slightly decreased to 87.8%, 86.8%, 84.5%, and 82.3% in the second, third, fourth, and fifth cycles, respectively. The gradual but minimal decline in performance indicates that the

photocatalyst retains a high level of activity over multiple cycles, demonstrating good stability and potential for practical applications. The minor reduction in efficiency could be attributed to partial surface fouling or minor loss of active sites during repeated use. In addition, the structural stability of the synthesized composite after the photoreaction was further evaluated using XRD analysis. As shown in the XRD patterns in Fig. S3, the characteristic diffraction peaks of the composite remain unchanged in position and intensity when compared to the unused photocatalyst, indicating that no phase transformation or structural degradation occurred during the photocatalytic process.

To evaluate the extent of mineralisation, Total Organic Carbon (TOC) analysis was performed after 60 minutes of visible-light irradiation using the BiOBr/30% $MgIn_2S_4$ heterojunction (Fig. S4). A TOC removal efficiency of 54% was obtained, indicating that more than half of the organic carbon in ciprofloxacin was converted into inorganic products. While the UV-Vis results showed 89.9% degradation of the parent compound, the lower TOC value suggests the formation of intermediate organic species that were not fully mineralised within the reaction time. The enhanced adsorption capacity observed for the BiOBr/$MgIn_2S_4$ composites can be directly correlated with their unique 2D/3D hierarchical morphology. SEM and TEM analyses reveal that the ultrathin BiOBr nanosheets are uniformly anchored onto the surface of the $MgIn_2S_4$ microspheres, leading to increased surface roughness and the exposure of additional active adsorption sites. This architecture also creates open interstitial spaces and short diffusion pathways, facilitating improved mass transfer and accessibility of ciprofloxacin molecules to the catalyst surface. Consequently, the composites exhibit higher adsorption capacity than the pristine materials, with the BiOBr/30%$MgIn_2S_4$ sample showing the most favourable balance between surface accessibility and interfacial contact.

3.6 Determination of reactive species

The experiment to trap radicals was conducted to determine the dominant ROS responsible for the degradation of CIP over the BiOBr/$MgIn_2S_4$ photocatalyst. As illustrated in Fig. 5e, the addition of Na-EDTA, a hole scavenger, caused a pronounced reduction in the degradation efficiency from 89.9% to 42%, suggesting that the photogenerated hole (h^+) plays the primary role in the degradation of CIP. Likewise, the addition of acrylamide lowered the degradation efficiency to 48%, showing that superoxide anion radical ($O_2^{\bullet-}$) is also a major contributor to the degradation process. In contrast, hydroxyl radical ($^{\bullet}OH$) plays a secondary role since the addition of isopropanol reduced the degradation efficiency to 72%.

4 Proposed heterojunction and photocatalytic mechanism

The results obtained from the Mott Schottky analysis were used to deduce an appropriate band diagram for BiOBr and $MgIn_2S_4$. In addition to the XPS analysis and radical testing experiment, it was confirmed that the VB and CB used for the degradation process must possess sufficient oxidation potential to directly oxidise CIP (~1.0–1.2 V) and produce $^{\bullet}OH$ ($^{\bullet}OH/H_2O = +2.26$ V), as well as sufficient reduction potentials to generate $O_2^{\bullet-}$ ($O_2/O_2^{\bullet-} = -0.33$ V). As illustrated in Fig. 5d, the band alignment of BiOBr and $MgIn_2S_4$ is the type II heterojunction. However, XPS shows that there is an increase in electron density around $MgIn_2S_4$, and the scavenger results show that the CB of $MgIn_2S_4$ and VB of BiOBr, with the highest reduction and oxidation, respectively, took part in the degradation process; hence, the formation of heterojunction did not follow the type II charge transfer mechanism.

Therefore, as displayed in Scheme 1, for a heterojunction to be formed, the Fermi level (E_f) of BiOBr and $MgIn_2S_4$ must align upon contact. To achieve this, electrons are transferred from BiOBr to $MgIn_2S_4$ as revealed by the XPS analysis, creating an electric field, leading to electron accumulation on $MgIn_2S_4$, thus making BiOBr hole-rich. Upon light radiation, photogenerated electrons and holes are generated in the CB and VB, respectively. The h^+ in the VB of $MgIn_2S_4$ and the e^- in the CB of BiOBr are relatively close to each other and can recombine easily, leaving behind the h^+ in the VB of BiOBr with sufficient potential to directly oxidise CIP or H_2O to generate $^{\bullet}OH$, and the e^- in the CB of $MgIn_2S_4$ with sufficient potential to reduce absorbed oxygen to $O_2^{\bullet-}$ (eqn 9–12). Therefore, the synergistic combination of 2D BiOBr and 3D $MgIn_2S_4$ forms a direct Z-scheme heterojunction, enabling spatially redox reactions where the highly oxidative and reductive holes and electrons, respectively, for efficient pollutant degradation.

$$\text{BiOBr/MgIn}_2\text{S}_4 + \text{Visible light} \rightarrow \text{BiOBr/MgIn}_2\text{S}_4\ (e^- + h^+) \quad (9)$$

$$h^+ + H_2O \rightarrow {}^{\bullet}OH + H^+ \quad (10)$$

$$e- + O_2 \rightarrow O_2^{\bullet-} \quad (11)$$

$$h^+ + O_2^{\bullet-}/{}^{\bullet}OH + \text{CIP} \rightarrow \text{Small molecules} \rightarrow CO_2 + H_2O \quad (12)$$

Table S3 shows how the BiOBr/$MgIn_2S_4$ heterojunction favourably compares with previously reported photocatalysts. Compared with previously reported photocatalytic heterojunction systems, the present BiOBr/$MgIn_2S_4$ photocatalyst offers distinct architectural and functional advantages arising from its 2D/3D configuration. The ultrathin BiOBr nanosheets provide abundant exposed reactive facets and short diffusion lengths for photogenerated holes, while the three-dimensional $MgIn_2S_4$hierarchical microspheres enhance visible-light harvesting through multiple light scattering and offer efficient electron transport pathways. This complementary structural integration maximizes the interfacial contact area and promotes the formation of a strong internal electric field at the interface. More importantly, the direct Z-scheme charge transfer pathway preserves the highly oxidative holes in BiOBr and the strongly reductive electrons in $MgIn_2S_4$overcoming the redox potential loss commonly associated with conventional type-II heterojunctions. As a result, the BiOBr/$MgIn_2S_4$ 2D/3D architecture achieves a synergistic enhancement in charge separation efficiency, redox capability, and photocatalytic

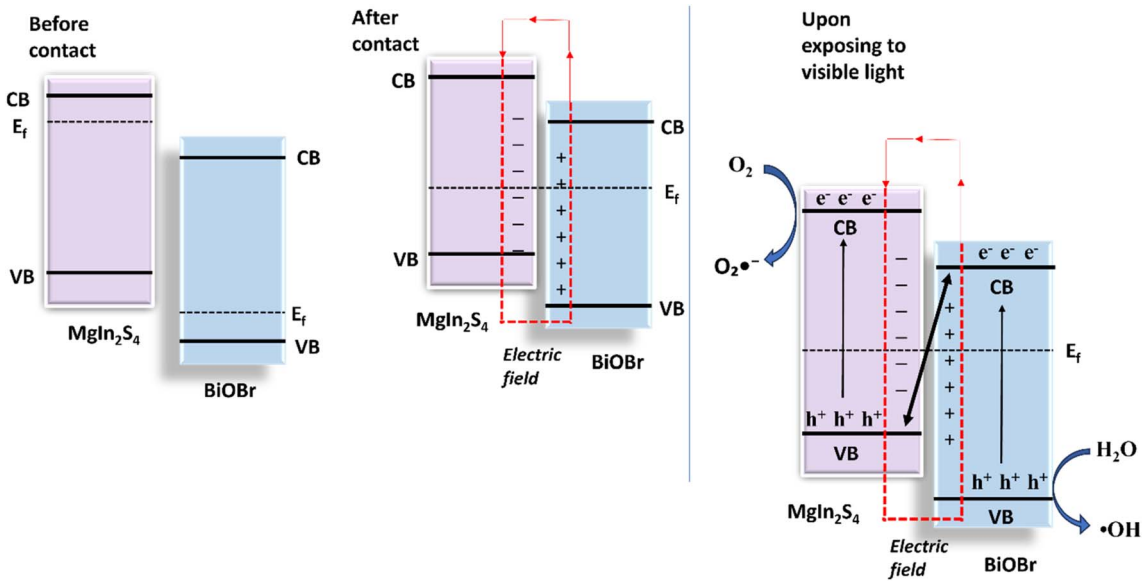

Scheme 1 Schematic illustration of heterojunction formation and photocatalytic mechanism.

stability, making it particularly effective for the degradation of recalcitrant antibiotics.

5 Conclusion

In conclusion, this work demonstrates the successful construction of a Z-scheme heterojunction *via* the *in situ* deposition of two-dimensional BiOBr onto three-dimensional $MgIn_2S_4$. Extensive morphological and structural analyses indicated that the strong interfacial contact between these photocatalysts was instrumental in promoting rapid charge transfer. The resultant synergistic effects led to enhanced visible light harvesting and superior charge carrier separation. Consequently, the BiOBr/30% $MgIn_2S_4$ photocatalyst exhibited peak performance, removing 89.9% of CIP in 60 minutes and demonstrating excellent recyclability with minimal loss of activity. These findings provide a valuable framework for developing advanced heterostructure photocatalysts for antibiotic degradation and other environmental applications. Beyond its high degradation efficiency and stability under visible light, the BiOBr/$MgIn_2S_4$ Z-scheme heterojunction holds promise as a versatile platform for advanced water treatment applications. The intimate 2D/3D interfacial architecture not only promotes efficient charge separation and strong redox capability but also provides a rational basis for further optimization toward practical deployment. Future efforts aimed at correlating surface properties with photocatalytic kinetics, elucidating degradation pathways and mineralisation behaviour at the molecular level, and validating performance in complex wastewater environments will be crucial for translating this material from laboratory-scale studies to real-world implementation. Overall, this work establishes a solid foundation for the rational design of next-generation Z-scheme photocatalysts capable of addressing persistent organic contaminants under sustainable, solar-driven conditions.

Conflicts of interest

There are no conflicts to declare.

Data availability

The data supporting this article have been included as part of the supplementary information (SI). Supplementary information is available. See DOI: https://doi.org/10.1039/d5ra07896b.

Acknowledgements

This work is supported by the African Research Universities Alliance (ARUA)/Carnegie Early Career Research Fellowship used at the University of Lagos and the University of Pretoria Research Development Program.

References

1 N. Morin-Crini, E. Lichtfouse, G. Liu, V. Balaram, A. R. L. Ribeiro, Z. Lu, F. Stock, E. Carmona, M. R. Teixeira, L. A. Picos-Corrales, J. C. Moreno-Piraján, L. Giraldo, C. Li, A. Pandey, D. Hocquet, G. Torri and G. Crini, Worldwide cases of water pollution by emerging contaminants: a review, *Environ. Chem. Lett.*, 2022, **20**, 2311–2338.

2 P. Sharma, L. Rani, A. S. Grewal and A. L. Srivastav, *Impact of Pharmaceuticals and Antibiotics Waste on the River Ecosystem: A Growing Threat, Ecological Significance of River Ecosystems*, Elsevier, 2022, pp. 15–36.

3 N. Talreja, C. Hegde, E. M. Kumar and M. Chavali, Emerging Environmental Contaminants: Sources, Consequences and Future Challenges, *Green Technologies for Industrial Contaminants*, 2025, pp. 119–149.

4 J. O. Tijani, O. O. Fatoba, O. O. Babajide and L. F. Petrik, Pharmaceuticals, endocrine disruptors, personal care products, nanomaterials and perfluorinated pollutants: a review, *Environ. Chem. Lett.*, 2016, **14**, 27–49.
5 D. Sharma, R. P. Patel, S. T. R. Zaidi, M. M. R. Sarker, Q. Y. Lean and L. C. Ming, Interplay of the Quality of Ciprofloxacin and Antibiotic Resistance in Developing Countries, *Front. Pharmacol*, 2017, **8**, 546.
6 N. Janecko, L. Pokludova, J. Blahova, Z. Svobodova and I. Literak, Implications of fluoroquinolone contamination for the aquatic environment—A review, *Environ. Toxicol. Chem.*, 2016, **35**, 2647–2656.
7 M. Patel, R. Kumar, K. Kishor, T. Mlsna, C. U. Pittman Jr and D. Mohan, Pharmaceuticals of Emerging Concern in Aquatic Systems: Chemistry, Occurrence, Effects, and Removal Methods, *Chem. Rev.*, 2019, **119**, 3510–3673.
8 A. Khalidi-Idrissi, A. Madinzi, A. Anouzla, A. Pala, L. Mouhir, Y. Kadmi and S. Souabi, Recent advances in the biological treatment of wastewater rich in emerging pollutants produced by pharmaceutical industrial discharges, *Int. J. Environ. Sci. Technol.*, 2023, 1–22.
9 E. M. Cuerda-Correa, M. F. Alexandre-Franco and C. Fernández-González, Advanced oxidation processes for the removal of antibiotics from water an overview, *Water*, 2019, **12**, 102.
10 J. Liu, R. Burciaga, S. Tang, S. Ding, H. Ran, W. Zhao, G. Wang, Z. Zhuang, L. Xie and Z. Lyu, Heterogeneous catalysis for the environment, *Innovation Mater.*, 2024, **2**, 100090.
11 L. Zhang, J. Zhang, H. Yu and J. Yu, Emerging S-Scheme Photocatalyst, *Adv. Mater.*, 2022, **34**, 2107668.
12 J. Low, J. Yu, M. Jaroniec, S. Wageh and A. A. Al-Ghamdi, Heterojunction photocatalysts, *Adv. Mater.*, 2017, **29**, 1601694.
13 L. Zhang and M. Jaroniec, Toward designing semiconductor-semiconductor heterojunctions for photocatalytic applications, *Appl. Surf. Sci.*, 2018, **430**, 2–17.
14 H. Yang, A short review on heterojunction photocatalysts: Carrier transfer behavior and photocatalytic mechanisms, *Mater. Res. Bull.*, 2021, **142**, 111406.
15 M. Bilal, M. Q. Alfaifi, S. B. Ahmed, M. M. Abduljawad, Y. I. Alrashed, E. S. Aldurahim and Y. A. Alassmy, A review of strategies to switch heterojunction system from type-II to S-scheme for photocatalytic applications, *Mater. Sci. Semicond. Process.*, 2025, **186**, 109051.
16 D. Salazar-Marín, G. Oza, J. A. D. Real, A. Cervantes-Uribe, H. Pérez-Vidal, M. K. Kesarla, J. G. T. Torres and S. Godavarthi, Distinguishing between type II and S-scheme heterojunction materials: A comprehensive review, *Appl. Surf. Sci. Adv.*, 2024, **19**, 100536.
17 J. Low, C. Jiang, B. Cheng, S. Wageh, A. A. Al-Ghamdi and J. Yu, A review of direct Z-scheme photocatalysts, *Small Methods*, 2017, **1**, 1700080.
18 K. D. Jayeola, D. S. Sipuka, T. I. Sebokolodi, J. O. Babalola, M. Zhou, F. Marken and O. A. Arotiba, Interfacial Engineering of a Z-Scheme Bi2O2S/NiTiO3 Heterojunction Photoanode for the Degradation of Sulfamethoxazole in Water, *ACS Appl. Mater. Interfaces*, 2024, **17**, 1385–1398.
19 T. L. Yusuf, B. O. Orimolade, D. Masekela, K. A. Adegoke, K. D. Modibane and S. S. Makgato, BiOX(X=Cl, Br, I)-based S-scheme heterostructure photocatalysts for environmental remediation and energy conversion, *Mater. Today Sustain.*, 2025, **30**, 101115.
20 L. Meng, Y. Qu and L. Jing, Recent advances in BiOBr-based photocatalysts for environmental remediation, *Chin. Chem. Lett.*, 2021, **32**, 3265–3276.
21 Z.-w. Zhang, R.-t. Guo, J. Tang, Y.-f. Miao, J.-w. Gu and W.-g. Pan, Fabrication of Bi-BiOCl/MgIn2S4 heterostructure with step-scheme mechanism for carbon dioxide photoreduction into methane, *J. CO_2 Util.*, 2021, **45**, 101453.
22 W. Chen, Y.-X. Hua, Y. Wang, T. Huang, T.-Y. Liu and X.-H. Liu, Two-dimensional mesoporous g-C3N4 nanosheet-supported MgIn2S4 nanoplates as visible-light-active heterostructures for enhanced photocatalytic activity, *J. Catal.*, 2017, **349**, 8–18.
23 D. C. Akintayo, T. L. Yusuf and N. Mabuba, Chalcogenide Materials in Water Purification: Advances in Adsorptive and Photocatalytic Removal of Organic Pollutants, *Small*, 2025, **21**, 2501378.
24 B. Luo, G. Liu and L. Wang, Recent advances in 2D materials for photocatalysis, *Nanoscale*, 2016, **8**, 6904–6920.
25 M. Cui, Q. Li, R. Bao, J. Xia and H. Li, 2D and 3D nanomaterials for photoelectrocatalytic removal of organic pollutants from water, *Cryst. Res. Technol.*, 2023, **58**, 2200195.
26 T. Senasu, S. Nijpanich, S. Juabrum, N. Chanlek and S. Nanan, CdS/BiOBr heterojunction photocatalyst with high performance for solar-light-driven degradation of ciprofloxacin and norfloxacin antibiotics, *Appl. Surf. Sci.*, 2021, **567**, 150850.
27 K. D. Jayeola, D. S. Sipuka, T. I. Sebokolodi, J. O. Babalola, Y. Zhao and O. A. Arotiba, Redistribution of charge in a 2D/1D BiOBr/Bi 2 O 2 S heterojunction for the photoelectrocatalytic oxidation of organic pollutants in water, *RSC Adv.*, 2025, **15**, 29680–29691.
28 H. Liu, C. Du, M. Li, S. Zhang, H. Bai, L. Yang and S. Zhang, One-Pot Hydrothermal Synthesis of SnO2/BiOBr Heterojunction Photocatalysts for the Efficient Degradation of Organic Pollutants Under Visible Light, *ACS Appl. Mater. Interfaces*, 2018, **10**, 28686–28694.
29 H.-Y. Liu, C.-G. Niu, H. Guo, C. Liang, D.-W. Huang, L. Zhang, Y.-Y. Yang and L. Li, In suit constructing 2D/1D MgIn2S4/CdS heterojunction system with enhanced photocatalytic activity towards treatment of wastewater and H2 production, *J. Colloid Interface Sci.*, 2020, **576**, 264–279.
30 Q.-Q. Fan, C.-G. Niu, H. Guo, D.-W. Huang, Z.-T. Dong, Y.-Y. Yang, H.-Y. Liu, L. Li and M.-Z. Qin, *J. Hazard. Mater.*, 2022, **438**, 129483.
31 C.-J. Jin, H.-Y. Niu, L. Ma, Y.-Y. Yang, L. Sui, Z.-T. Dong, Y.-R. Peng, M. Yan and C.-G. Niu, *Chem. Eng. J.*, 2025, **523**, 168769.

32 L. Li, M. A. Boda, C. Chen, F. Wang, Y. Liu and Z. Yi, BiOBr Micro–Nanosheets: Controllable Synthesis and Piezoelectric and Photoelectric Properties, *Cryst. Growth Des.*, 2021, **21**, 7179–7185.

33 D. C. Akintayo, T. L. Yusuf and N. Mabuba, Construction of hierarchical S-scheme MgIn2S4/CeO2 heterojunction for boosted photocatalytic oxidation of tetracycline and reduction of Cr(VI), *Colloids Surf., A*, 2025, **721**, 137215.

34 A. Lodh, K. Thool and I. Samajdar, X-ray Diffraction for the Determination of Residual Stress of Crystalline Material: An Overview, *Trans. Indian Inst. Met.*, 2022, **75**, 983–995.

35 M. T. Ulhakim, S. Sukarman, K. Khoirudin, N. Fazrin, T. Irfani and A. Hakim, Determining the crystallite size of TiO2/EG-water XRD data using the Scherrer equation, *Indones. J. Appl. Phys.*, 2024, **14**, 141–150.

36 X. Wang, L. Sø, R. Su, S. Wendt, P. Hald, A. Mamakhel, C. Yang, Y. Huang, B. Iversen and F. Besenbacher, The influence of crystallite size and crystallinity of anatase nanoparticles on the photo-degradation of phenol, *J. Catal.*, 2014, **310**, 100–108.

37 X. Miao, K. Pan, Y. Liao, W. Zhou, Q.-J. Pan, g. Tian and W. Guofeng, Controlled synthesis of mesoporous anatase TiO2 microspheres as scattering layer to enhance photoelectrical conversion efficiency, *J. Mater. Chem. A*, 2013, **1**(34), 9853–9861.

38 Z. M. Detweiler, S. M. Wulfsberg, M. G. Frith, A. B. Bocarsly and S. L. Bernasek, The oxidation and surface speciation of indium and indium oxides exposed to atmospheric oxidants, *Surf. Sci.*, 2016, **648**, 188–195.

39 A. C. Lazanas and M. I. Prodromidis, Electrochemical Impedance Spectroscopy-A Tutorial, *ACS Meas. Sci. Au*, 2023, **3**, 162–193.

40 S. Ashu Abey, N. M. Reis, E. A. C. Emanuelsson and A. J. Expósito, Harnessing visible light: Advanced photocatalytic strategies for sustainable environmental reactions, *Chem. Eng. J.*, 2025, **519**, 164951.

41 Q. Li, M. Anpo, J. You, T. Yan and X. Wang, Photoluminescence (PL) Spectroscopy, in *Springer Handbook of Advanced Catalyst Characterization*, ed. I. E. Wachs and M. A. Bañares, Springer International Publishing, Cham, 2023, pp. 295–321.

42 A. P. Chowdhury and B. H. Shambharkar, Fabrication and characterization of BiOBr-SnWO4 heterojunction nanocomposites with boosted photodegradation capability, *Chem. Eng. J. Adv.*, 2020, **4**, 100040.

43 T. L. Yusuf, O. C. Olatunde, D. Masekela, K. D. Modibane, D. C. Onwudiwe and S. Makgato, Charge Redistribution in $Nise_2/Mos_2$ n–n Heterojunction Towards the Photoelectrocatalytic Degradation of Ciprofloxacin, *ChemElectroChem*, 2024, **11**(16), e202400309.